DESY 10-225
November 2010
ISSN 0418-9833

Design and Construction of a Cherenkov Detector for Compton Polarimetry at the ILC

arXiv:1011.6314v1 [physics.ins-det] 29 Nov 2010

Christoph Bartels[1,2], Joachim Ebert[2], Anthony Hartin[1], Christian Helebrant[1], Daniela Käfer[1], and Jenny List[1]

1- Deutsches Elektronen-Synchrotron DESY
Notkestr. 85, 22607 Hamburg, Germany

2- Universität Hamburg, Institut für Experimentalphysik
Luruper Chaussee 149, 22761 Hamburg, Germany

Abstract

This paper describes the design and construction of a Cherenkov detector conceived with regard to high energy Compton polarimeters for the International Linear Collider, where beam diagnostic systems of unprecedented precision must complement the interaction region detectors to pursue an ambitious physics programme. Besides the design of the Cherenkov detector, detailed simulation studies and first testbeam results are presented. Good agreement of beam data with expectations from Monte Carlo simulations is observed.

To be submitted to Nucl. Instrum. Meth. **A**

1 Introduction

The measurement and control of beam parameters to permille level precision will play an important role in the physics programme [1, 2] of the International Linear Collider (ILC). For electroweak processes, the absolute normalisation of expected event rates depends on both, luminosity and polarisation. The luminosity will be measured to a precision of 10^{-3} to 10^{-4}, while for the luminosity weighted polarisation average an accuracy of 10^{-3} seems achievable.

While for beam energy and luminosity measurements the ILC's precision goals have already been achieved at previous colliders, polarimetry has to be improved by at least a factor of two compared to the most precise previous measurement of the SLD polarimeter [3].

The polarisation determination at the ILC will combine the measurements of two dedicated Compton polarimeters, located upstream and downstream of the e^+e^- interaction point, and data from the e^+e^- annihilations themselves. While the annihilation data will finally yield the absolute polarisation scale, the polarimeters provide fast measurements which allow to track variations over time and to detect possible correlations with the luminosity or the polarisation of the other beam. Therefore, each polarimeter has to reach a systematic accuracy of at least $\delta\mathcal{P}/\mathcal{P} = 0.25\%$. Two polarimeters per beam are required in order to measure the polarisation of the beams in collisions. Both polarimeters have been designed for operation at beam energies between 45 GeV and 500 GeV. A detailed description of the polarimeters can be found in [4].

Both polarimeters make use of the polarisation dependence of Compton scattering to ensure a non-destructive measurement of the longitudinal beam polarisation. Circularly polarised laser light is shot under a small angle onto the individual bunches causing typically in the order of 10^3 electrons[1] per bunch to undergo Compton scattering. The energy spectrum of these scattered particles depends on the product of laser and beam polarisations, so that the differential rate asymmetry with respect to the laser helicity is directly proportional to the beam polarisation. Since the scattering angle in the laboratory frame is less than 10 μrad, a magnetic chicane is used to transform the energy spectrum into a spatial distribution which is then measured by Cherenkov detectors.

A Cherenkov detector was chosen for several reasons:

(i) In combination with the magnetic chicane, it allows to measure the energy spectrum of many electrons arriving simultaneously. With about 10^3 Compton interactions per electron bunch, a statistical precision of 1% is achieved for each of the about 3000 bunch position in a train after only 4 seconds. For the average polarisation of all bunch positions, this corresponds to a statistical error below 0.1% after 1 second [4].

(ii) For relativistic electrons ($\beta = v/c \approx 1$), Cherenkov radiation is independent of the electron energy. Thus, the number of Cherenkov photons will be directly proportional to the number of electrons per detector channel.

[1] or positrons in case of the positron beam of the ILC which is equipped analogously.

(iii) Typical Cherenkov media like gases or quartz are sufficiently radiation hard to withstand the flux of 10^7 electrons passing through the detector per second.

Developing a Cherenkov detector suitable for achieving the target precision of $\delta\mathcal{P}/\mathcal{P} = 0.25\%$ demands improvements in various areas of the experimental setup. The requirements on the detector have been evaluated and according to these, a prototype detector has been designed, simulated and constructed. This prototype allows nearly all aspects of the final detector to be studied and has been operated successfully in a testbeam.

In the next chapter, design and simulation studies are discussed, followed by a chapter dedicated to the construction of the prototype and the last chapter presents results of the testbeam campaign.

2 Detector Design and Simulation

A conceptual design for the Cherenkov detector envisioned for the ILC polarimeters is shown in Figure 1(a). It will consist of staggered 'U-shaped' aluminium channels lining the tapered exit window of the beam pipe. They are filled with a Cherenkov gas so that relativistic electrons traversing their base emit Cherenkov radiation which is reflected upwards in the hind U-leg to the photodetectors. A single channel is sketched in Figure 1(b). The requirements leading to this design, which has been developed based on the one proposed in [5], will be discussed in this chapter.

The wavelength spectrum of Cherenkov radiation is given by:

$$\frac{dN^\gamma}{d\lambda} = 2\pi\alpha \left(1 - \frac{1}{n^2\beta^2}\right) \frac{1}{\lambda^2}\,\ell\,, \qquad \text{with:} \quad \begin{array}{ll} N^\gamma & : \text{number of photons,} \\ \lambda & : \text{wavelength,} \\ \alpha & : \text{fine structure constant,} \\ n & : \text{radiator's refraction index,} \\ \beta & : \text{velocity } (\beta = \frac{v}{c}), \\ \ell & : \text{radiator length} \end{array} \tag{1}$$

While the velocity (β) can be regarded as constant for electron energies relevant at the ILC, the refraction index depends on the wavelength, as well as on the temperature and the gas pressure. At small wavelengths, the refraction index typically rises like $(n-1) = A/[\lambda_0^{-2} - \lambda^{-2}]$. This behaviour has been measured for C_4F_{10} for the Ring Imaging Cherenkov Detector of the DELPHI experiment at LEP [6]. Furthermore, $n-1$ is proportional to the number density of molecules for $n \approx 1$ [7] and thus increases proportionally with the inverse temperature and the pressure.

To simplify further references, a right-handed coordinate system, as shown in Figure 1, will be used throughout the rest of this publication. Assuming the electron beam travels in positive z direction, the y-axis points upwards, and the x-axis to the left when looking in the direction of the electron beam.

2.1 Requirements and conceptual design

The design of the Cherenkov detectors for the ILC polarimeters is driven by the following requirements:

High and homogenous light yield
Since Cherenkov radiation is characterised by a $1/\lambda^2$ distribution, high reflectivity at short wavelengths of $\lambda \approx 200 - 350\,\mathrm{nm}$ is required in order to obtain a high light yield per Compton electron and thus keep fluctuations small. All relevant detector surfaces should be manufactured as smooth and planar as possible to ensure a uniform light transmission to the photodetector. Furthermore, a channel geometry which leads to a homogeneous illumination of the photodetector is desirable.

Gas- and light-tightness
In order to control the linearity to permille level accuracy and to achieve a stable response, it is indispensable for the entire detector system to be light- and gas-tight. The detector should be sufficiently tight to keep a stable pressure over several weeks without a permanent gas flow system.

Thin walls between channels
Electrons entering the channel walls are not only lost for Cherenkov detection, but might also initiate an electromagnetic shower and thus create background in the adjacent channels. Therefore the walls should be as thin as possible.

Robustness with respect to backgrounds
A gas with a Cherenkov threshold in the MeV-regime should be used to avoid the emission of Cherenkov light from low energetic electrons and muons, e.g. from the beam halo, from beam-gas interactions, or electrons pair-produced from synchrotron radiation. A layout allowing the photodetectors and electronics to be placed well outside the beam-plane is mandatory.

Calibration system
A dedicated calibration system is forseen to monitor the detector response, especially its linearity, in-situ. This could be realised by equipping the channels with light emitting diodes (LEDs) which should also be placed outside the beam-plane. Such a system could collect data during breaks in the accelerator operation, or even in-between two ILC bunch trains.

The last two requirements are satisfied by the U-shaped channels depicted in Figure 1. With increasing length of the U-base more Cherekov light is produced, but on the other hand the alignment requirements become more stringent and additional reflections will decrease the light yield. Simulations suggest that a length of 15 cm is a reasonable choice.

In order to test the realisation of the above requirements, a prototype Cherenkov detector has been constructed. In contrast to the ILC-like design of 20 staggered channels (c.f. Figure 1(a)), the prototype detector consists of two parallel, non-staggered channels. Apart from this difference, the smaller prototype detector allows to test all relevant aspects of the full detector.

2.2 Optical simulation

A detailed simulation of the prototype detector based on GEANT4 [8] has been created in order to support the design process and the interpretation of the testbeam data.

For electrons and positrons Cherenkov radiation, multiple scattering, ionisation, bremsstrahlung and annihilation are simulated. Apart from annihilation, the same processes are taken into account for muons, which are relevant when studying the impact of accelerator background. For the Cherenkov photons optical processes have to be considered since their wavelengths are much larger than a typical atomic spacing. In particular, absorption in the photodetector entrance window, boundary effects (like reflection and absorption) at the channel walls, as well as Rayleigh elastic scattering have been included in the simulation [9].

As Cherenkov gas, perfluorobutane (C_4F_{10}) has been chosen due to its high threshold of 10 MeV, which makes the detector robust against background from low energetic charged particles. The refraction index has been assumed to be $n = 1.0014$ independent of the wavelength, which underestimates the number of photons in the far UV region. Since the polarisation measurement is based on rate asymmetries, it will be insensitive to the exact value of n. Also variations of n which are slow with respect to the laser helicity flipping rate (like thermal variations) will cancel from the asymmetry. Therefore such effects are currently not simulated and the temperature and gas pressure inside the detector box are set to $T = 20\,^{\circ}\mathrm{C}$ and $p = 1\,\mathrm{atm} = 1.01325\,\mathrm{bar}$, respectively.

Pure C_4F_{10} is fully transparent even in the far UV range. In the presence of impurities, especially water or oxygen, the transparency can drop significantly for wavelengths smaller than 200 nm [6], where two of the four employed photodetectors are sensitive, c.f. Section 3.1. Since the precise knowledge of the absolute photon yield is not crucial for the rate asymmetry measurement, gas impurities have not been implemented in the simulation.

Two different types of aluminium have been implemented in the simulation according to the reflectivity studies summarised in Section 2.5. The wavelength dependency is interpolated linearly between the values listed in Table 1. Three of the four walls of each channel are made of diamond-milled aluminium, while the inter-channel wall consists of a 300 µm thin foil of rolled aluminium with less than half the reflectivity of diamond-milled aluminium.

Figure 2 shows the channel structure with a single electron (red line) passing from left to right through the U-base of the right-hand side channel. It emits Cherenkov light (green), which is reflected upwards at the end of the U-base towards the photodetector. Cherenkov light produced outside the channel structure in the ambient gas cannot reach the photodetectors. The optical simulation ends at the photocathode and all Cherenkov spectra are stored for further processing and digitisation.

2.3 Cherenkov spectra and light distributions

The number of emitted Cherenkov photons follows a Poisson distribution with the most probable value N given by the integral of formula 1 over the relevant wavelength range.

The number of photons reaching the photocathode is expected to follow a Poisson distribution as well, if only small, homogeneous losses occur.

To study the influence of the detector geometry and the reduced reflectivity of the inter-channel wall on the expected light distribution, the simulation has been run twice with the same beam parameters but different reflectivities for the inter-channel wall. The beam profile has been chosen as a two-dimensional Gaussian with standard deviations $\sigma_x = \sigma_y = 0.5$ mm, and the electrons enter the Cherenkov volume centred on one of the two channels. For each scenario, 10^5 electrons with an energy of 2 GeV have been simulated.

Figure 3 shows the number of Cherenkov photons at the photocathode for both cases: In Figure 3(a), all channel walls have been simulated with the reflectivity of diamond-milled aluminium, resulting in on average 64.7 photons per Compton electron. When the reflectivity of the inter-channel wall is reduced to the level measured for the rolled foil, about 24% less photons reach the photocathode, so that the average decreases to 52.1 photons as shown in Figure 3(b).

Due to the sufficiently large number of photons, both distributions can be approximated by Gaussians with a mean value of N and a variance of $\sqrt{N}$. The actual variances obtained from Gaussian fits to the simulated distributions are slightly larger than the ideal value of $\sqrt{N}$, indicating that indeed only small losses occur.

Figure 4 shows the wavelength spectrum of these photons obtained from the simulation with the reduced reflectivity for the inter-channel wall. Figure 4(a) illustrates the distribution at the photocathode, showing the expected $1/\lambda^2$ wavelength dependence for Cherenkov radiation. It is cut off below $\lambda_{\text{low}} = 160$ nm and above $\lambda_{\text{high}} = 900$ nm in the simulation since the photodetectors are not sensitive outside this wavelength range. Figure 4(b) shows the wavelength spectrum after convolution with the quantum efficiency of the 2×2 multi-anode photodetector (Hamamatsu R7600U-03-M4). This quantum efficiency is shown in the insert in Figure 4(a) [13]. On average, 6.5 photons are detected corresponding to the integral of the histogram in Figure 4(b).

Figure 5 shows the resulting spatial light distributions on the photocathode. The result obtained with equal reflectivities for all inner surfaces is illustrated in Figure 5(a). In this case, the observed inhomogeneities are due to the influence of the detector geometry. For reference a white dot indicates the position of the channel centre. The distribution exhibits an X-like structure of increased photon yield which is symmetrical about the x and z-axes. A reduced light yield is visible in two narrow bands at $z = \pm1$ mm as residuals from the 90° reflection at the end of the Cherenkov section. Lowering the reflectivity of the inter-channel wall (located at $x = -4.25$ mm) changes the symmetry of the light pattern as shown in Figure 5(b). Near the inter-channel wall, the light yield is reduced, but the X-like structure remains.

These features can be understood with the sketches in Figure 6, which illustrate two cases of photocathode illumination for an electron traversing the channel along its central axis and assuming the Cherenkov angle of the chosen gas ($\Theta = 3°$). Photons emitted in the horizontal (or vertical) plane illuminate the entire width of the channel at the photocathode as shown in Figure 6(a). Due to the larger effective channel cross section, photons

emitted towards the corners illuminate only half the channel width at the photocathode as illustrated in Figure 6(b). This leads to a higher photon yield near the diagonals of the channel cross section which also explains the X-like structure observed in Figure 5. In addition, Figure 6(b) explaines the fact that the lower reflectivity of the inter-channel wall leads to a depletion on the same side of the channel.

2.4 Yield asymmetries and beam position

The light distribution on the photocathode has been simulated for a grid scan of 4×4 beam positions with 10^4 electrons per position. Figure 7(a) depicts the light yield on the photocathode for electrons entering the Cherenkov section at a fixed y-position and four different x-positions. The y-position of the beam, indicated by the white dots in Figure 7(a), translates directly to the z-position in the readout plane of the photodetector.

The asymmetries in Figures 7(b,c) are calculated from the light intensities for scans in the x and z directions, respectively. For each beam position the corresponding asymmetries are defined as

$$A_x = \frac{I_x^+ - I_x^-}{I_x^+ + I_x^-} \qquad \text{and} \qquad A_z = \frac{I_z^+ - I_z^-}{I_z^+ + I_z^-} \ ,$$

where I_x^+ (I_z^+) corresponds to the intensity in the right (upper) half of a channel and I_x^- (I_z^-) to the intensity in the left (lower) half, respectively.

These asymmetries have an approximately linear dependence on the beam position. The non-zero value of A_x at $x = 0$ visible in Figure 7(b) originates from the lower reflectivity of the inter-channel wall corresponding to the clear asymmetry in Figure 5(b). This effect does not exist in case of A_z displayed in Figure 7(c), since the upper and lower channel walls have the same reflectivity. In addition, the lower reflectivity of the inter-channel wall leads to a more shallow slope of A_x compared to A_z.

For comparison the same asymmetries have been simulated for equal reflectivities of all channel walls as shown in Figure 8. The offset in the x-asymmetry, visible in Figure 7(b) is not observed in Figure 8(a) and A_x and A_z have the same slope. Also, the slight variations of the z-asymmetry for different x-positions at extreme values of z do not occur in case of equal reflectivities for all channel walls, see Figure 8(b).

2.5 Reflectivity measurements

When choosing the detector materials, different qualities of aluminium have been considered, primarily with regard to their reflectivity, but also concerning smoothness and mechanical stability.

Reflectivity measurements of small aluminium probes (blocks, sheets, and sub mm-foils) of different quality have been performed with a modified transmission spectrometer [14]. The path of the measurement beam inside the spectrometer has been changed such that it reflects off four small blocks instead of passing through the probe material, as shown

in Figure 9(a). One photomultiplier detects the previously splitted reference and measurement beams and thus provides a measure of how much light is reflected by the four blocks' surfaces with respect to the reference beam. Since the spectrometer was originally designed for transmission measurements, only lower limits on the reflectivity can be derived.

With four diamond-milled aluminium blocks a total reflectivity of $R_{\text{diam}} \gtrsim 80\%$ is observed for wavelengths above $\lambda \geq 200\,\text{nm}$, shown as the upper black line in Figure 9(b). All inner surfaces of the Cherenkov detector channels are diamond-milled with the exception of the 0.3 mm-thin inter-channel wall, which consists of rolled aluminium foil purchased from GoodFellow[2]. The measured reflectivity of the rolled foil $R_{\text{roll}} \gtrsim 30\%$ is considerably lower than for the diamond-milled surfaces, as shown by the lower grey line in Figure 9(b).

The reflectivity of the inter-channel wall should be improved for the final detectors in order to obtain a homogeneous light yield. However, in the prototype, the different reflectivities provided the opportunity to cross check the simulation.

3 Construction of the Prototype

The channel dimensions of the prototype were chosen to match the design criteria discussed in section 2.1. The length of the U-base relevant for the emission of Cherenkov radiation from traversing electrons is 150 mm and the height of the two U-legs is 100 mm. A quadratic cross section of $8.5 \times 8.5\,\text{mm}^2$ has been chosen to match the cathode geometry of two square multi-anode photomultipliers. Section 3.1 gives further details of the employed photodetectors and their characteristics.

The size of the outer box is $230 \times 90 \times 150\,\text{mm}^3$ (L×W×H) allowing for easy accomodation of the channel structure. Parts of the technical drawing, e.g. the channel structure and its placement inside the box, are shown in Figure 10.

Perfluorobutane was chosen as Cherenkov gas due to its high Cherenkov threshold of about 10 MeV for electrons. In addition it is neither flammable, nor explosive, contrary to propane or isobutane. The 10 mm thick aluminium lid of the box holds an electronic pressure gauge suited for remote read-out. The entrance and exit windows for the electron beam consist of 0.5 mm thin aluminium sheets.

All mountings for LEDs, photodetectors and windows have been designed to be gas- and light-tight, as well as easily exchangeable.

3.1 Photodetectors and their mountings

The hind U-leg can be equipped with four different types of photodetectors, which are listed in Table 2 along with some of their characteristics. They differ in geometry (square

[2]GoodFellow GmbH, Germany; Aluminium foil: AL000601 (thickness: 0.15 mm, purity: 99.0%, hardness: hard)

versus round) and the number of anode pads as illustrated in Figure 11. Their gains are in the order of 10^6 with wavelength thresholds between 160 nm and 300 nm and their response times range from 6.5ns to 28ns. In case of the square multi-anode photodetectors (MAPMs), one quadrant of their cathodes exactly matches one detector channel. Thus, both detector channels can be read out simultaneously by the same photodetector.

While the round single-anode photodetectors (SAPMs) are inserted into their respective mountings using appropriate O-ring seals, the MAPMs need to be glued into their mountings. Epoxy resin mixed with black paint was used as glue to ensure gas- also light-tightness. The mountings themselves were manufactured from poly-oxy-methylene (POM) for electrical insulation. They provide for three different photodetector positions relative to the detector channels as depicted in Figure 12. In addition, both MAPM mountings can be rotated by 180° for systematic studies.

3.2 LED calibration system

The front U-leg of the detector serves for calibration purposes and is equipped with one LED per channel. The LEDs have a peak wavelength of 470 nm (HLMP-CB30-NRG, Agilent Technologies [16]) and are glued into their mounting structure using epoxy resin.

As shown in Figure 13, two slender 18 mm long POM tubes encase the LEDs to ensure that the light from one LED does not enter the neighbouring channel through a small slit in the inter-channel wall necessary for gas circulation. A temperature sensor is placed in between the two POM tubes to allow for temperature monitoring.

3.3 Additional components

Two small, light-tight boxes protect the MAPMs and their electrical bases. A rotation mechanism on a plastic base plate allows to adjust the detector's horizontal tilt about the y-axis in reproducible steps of 0.125° between $\alpha_y = \pm 3.0°$. The fixed rotational axis lies in the center of the front U-leg as illustrated in Figure 10(b).

4 Beam Tests at the ELSA Accelerator

Beam tests with the prototype detector were performed in an external beam line at ELSA. The ELektronen-Stretcher-Anlage (ELSA) is an electron accelerator consisting of three stages: injector LINACs, a booster synchrotron and the stretcher ring [17]. A beam of polarised or unpolarised electrons of variable energy up to 3.5 GeV can be stored and used for various experiments in different beam line areas around the storage ring. The stretcher ring has a circumference of 164.4 m corresponding to a turn time of 548 ns. The ELSA beam is structured by the RF frequency of 500 MHz. Of 274 buckets in total, a variable fraction can be filled. As an example, Figure 14 shows the fill structure for four 548 ns turns of the partially filled ELSA accelerator.

4.1 Setup and first signals

During the testbeam period, ELSA was operated in *booster mode* with the electrons being injected at an energy of 1.2 GeV and subsequently accelerated to 2.0 GeV. The beam is extracted in intervalls of 4.0 s for every 5.1 s cycle and can be focussed to a beam spot size of about 1 mm to 2 mm. The extraction current is adjustable from approximately 10 pA to 200 pA leading to respectively 35 to 700 electrons traversing the detector per ELSA turn. In comparison, up to 250 electrons per bunch crossing are expected in the most populated channel of a polarimeter Cherenkov detector at the ILC.

The beam clock signal was used to provide the gate for the QDC (charge sensitive analog-to-digital converter), as illustrated in the block diagram of the readout chain in Figure 15. The gate width was adjusted between 100 ns and 480 ns to integrate over the filled part of one ELSA turn.

The detector was filled with the Cherenkov gas C_4F_{10} at a slight overpressure of about 140 mbar. This overpressure remained stable although frequent changes to the setup prevented a monitoring of the gas pressure for continuous time periods longer than two weeks. Figure 16 shows the Cherenkov detector set up in one of the ELSA external beam lines, directly behind a dipole magnet bending the electrons by $\approx 7.5^\circ$ towards a downstream beam dump. The detector was mounted on its base plate (black) and additionally affixed to a stage moveable along the x- and y-axis. The two angles, α_x and α_z, had to be adjusted using a water-level.

One of the first measurements performed with beam is illustrated in Figure 17. The filled grey histogram in Figure 17(a) depicts the QDC response with no bias voltage applied to the photodetector (pedestal) and without ELSA operation, while the open histograms show the QDC response for a bias voltage of 400V applied to the photodetector (dark current). The dark (light) colour corresponds to the case without (with) beam circulating in ELSA. All three histograms are normalised to the same number of entries. Both, the photodetector dark current and the accelerator operation, lead to a slight broadening of the pedestal peak, but its position remains stable. This is illustrated further by Figure 17(b) which shows again a dark current signal (filled grey histogram) recorded while beam was circulating in ELSA, and, in addition, Cherenkov signals for three different extraction currents (open coloured histograms). Besides the beam signals, each open histogram features a small peak coinciding with the pedestal position because the data taking continued during the 1.1 s of filling and acceleration. This provides the opportunity to monitor the pedestal stability continuously during beam operation. The relative areas of beam signal and pedestal peaks reflect the $4:1$ ratio defined by the 5.1 s-periodic cycle of extraction and refill/acceleration times. All following Figures show pedestal-subtracted signals.

4.2 Alignment and control measurements

The alignment of the detector with respect to the electron beam line was obtained from beam data. By moving the detector stage, the incident beam position on the entrance

window was scanned in horizontal (x) and vertical (y) directions. The adjustment procedure requires one vertical scan for each detector channel and a series of horizontal scans across both channels for different tilt angles α_y, as shown in Figure 18.

When the detector is tilted, the electrons will not have the full channel length to produce Cherenkov light. The maximal signal for any given x position of the beam will be smaller than for a perfectly aligned detector [3]. For each tilt angle, the beam x position resulting in the highest signal is determined as displayed in Figure 18. The best alignment of the detector with respect to the beam line is achieved for a tilt angle of $\alpha_y = (1.33 \pm 0.03)^\circ$. Due to the step size of the rotation mechanism, this value was approximated to $\alpha_y = 1.35^\circ$ for all following measurements.

4.2.1 Measurements with the R7600U-03-M4 and R7400U-06 photodetectors

The first complete measurement series was performed with the 2×2 multi-anode photomultiplier (R7600U-03-M4) positioned on the detector channels as illustrated in Figure 12(c). Figure 19(a) shows the results of an x-scan across both detector channels and for a tilt angle of $\alpha_y = 1.35^\circ$ adjusted according to the step size of the rotation mechanism. Two Gaussian fits indicate the respective channel centres to be at $x_{\text{right}} = (7.4 \pm 0.1)$ mm and $x_{\text{left}} = (16.4 \pm 0.1)$ mm, leading to a distance of $\Delta x = (9.0 \pm 0.2)$ mm. This agrees with the nominal distance between the channel centres of $\Delta x_{nom} = 8.8$ mm, given by the width of one channel and the inter-channel wall.

Figure 19(b) shows x-scan data for the single-anode photomultiplier R7400U-06, where a broad plateau is observed. The width of the signal region is determined from two sigmoidal fits to the edges of the plateau. At 50% of the plateau height, this width is found to be $w = (9.4 \pm 0.3)$ mm, where the error is dominated by the table position accuracy. This value is larger than the nominal width, $w_{nom} = 8.5$ mm, hinting towards residual misalignment and a non-Gaussian beam profile.

The x-scan in Figure 19(a) for the 2×2 MAPM does not exhibit such a clear plateau as for the SAPM in Figure 19(b). In addition to a possible contribution from cross-talk in case of the MAPM and the incomplete channel coverage of the SAPM, the dominant reason for this effect are the different beam spots delievered by ELSA. Figure 20 shows photographs of a fluorescent screen placed on the detector entrance window for two typical situations: Figure 20(a) shows a very elongated beam spot observed at the time the MAPM data were recorded (Fig. 19(a)), while the significantly smaller and nearly round beam spot shown in Figure 20(b) was achieved during data taking with the SAPM (Fig. 19(b)).

4.2.2 Measurements with the R7600-00-M64 photodetector

The anode of the 8×8 multi-anode photomultiplier (R7600-00-M64) is finely segmented with 16 anode pads covering a single Cherenkov channel, thus offering spatial resolution within a detector channel. Since two QDC channels were broken, only six channels were

[3] Due to the channel geometry, this holds for all tilt angles larger than 0.027°.

available to realise the readout configuration illustrated in Figure 21. The numbers indicate the QDC channel utilised to read out the sum signal of either four or eight anode pads of the photodetector.

Figure 22 shows the results of (a) an x-scan across both detector channels and (b) the corresponding y-scan across the left channel. As expected, the signals in QDC channels 2 and 3 are about twice as large as in the other channels since eight instead of only four anode pads are grouped together. The asymmetric response reflects the incident beam position. For each QDC channel, the largest signal is observed when the beam enters on the opposite side of the detector channel. This confirms the prediction of one glancing angle reflection for most of the photons obtained from MC simulations (c.f. Section 2.3 and 2.4).

For a more detailed comparison of the responses of the different anode segments, the same data are displayed again in Figure 23, scaled and mirrored to correct for the two above effects. Possible reasons for the remaining shape and amplitude differences comprise gain variations between the pads and residual detector misalignment.

4.3 Asymmetry analysis

From the measurements with the 8×8 MAPM discussed in the previous section, the x- and z-asymmetries are calculated as described in section 2.4. Only the four readout channels QDC 4 to QDC 7 are used (c.f. Figure 21). Two x-asymmetries, A_x^{lower} and A_x^{upper}, are calculated for QDC channels 4+5 and QDC channels 6+7, while the orthogonal grouping of QDC channels 5+6 and QDC channels 4+7 gives the respective z-asymmetries, A_z^{left} and A_z^{right}.

x-asymmetries:

$$A_x^{lower} = \frac{\mathrm{QDC\,5} - \mathrm{QDC\,4}}{\mathrm{QDC\,5} + \mathrm{QDC\,4}}$$

$$A_x^{upper} = \frac{\mathrm{QDC\,6} - \mathrm{QDC\,7}}{\mathrm{QDC\,6} + \mathrm{QDC\,7}}$$

z-asymmetries:

$$A_z^{left} = \frac{\mathrm{QDC\,6} - \mathrm{QDC\,5}}{\mathrm{QDC\,6} + \mathrm{QDC\,5}}$$

$$A_z^{right} = \frac{\mathrm{QDC\,7} - \mathrm{QDC\,4}}{\mathrm{QDC\,7} + \mathrm{QDC\,4}}$$

The resulting asymmetries are displayed in Figure 24, together with the simulated ones. The displayed errors correspond to 10% relative gain differences between the anode pads. Uncertainties which are in common between the different pads cancel from the asymmetries. Qualitatively the measured asymmetries agree well with the expectation from simulation. Especially the x-asymmetries exhibit a clear offset in x and a more shallow slope as expected due to the lower reflectivity of the inter-channel wall. This demonstrates the optical quality of the channel walls and a sufficiently detailed description in the simulation. Quantitatively, some of the measured asymmetries deviate from the ideal expectation. The x-asymmetry A_x^{upper} from QDC channels 6 and 7 exhibits a different slope, while the z-asymmetry A_z^{right} from QDC channels 4 and 7 seems to be shifted. These differences suggest residual misalignment and gain variations. In any case, if a segmented photodetector is employed in the final detector, these asymmetries would offer the possibility to determine the beam position even within a single detector channel.

5 Conclusions

At a future e^+e^- linear collider, Compton polarimeters will be employed to measure the beam polarisation to a precision of $\delta\mathcal{P}/\mathcal{P} = 0.25\%$, using Cherenkov detectors to register the scattered Compton electrons.

A compact two channel prototype detector has been designed and constructed. This prototype allows nearly all aspects of the final detector to be studied. In addition, it has been designed for easy exchange of the photodetectors and the calibration light source.

The prototype has been operated successfully in a testbeam using four different photodetectors. The corresponding results are in good agreement with a detailed simulation. In particular, a method to extract intra-channel beam position information has been developed. Furthermore, the detector response has been studied as a function of the beam position. This will lead to a determination of each channel's acceptance which is important to control systematic effects on the final polarisation measurements.

In the future it is planned to use this prototype to compare different photodetectors and to establish a calibration to the permille level as required for the ILC.

Acknowledgements

We thank C. Hagner and R. Klanner of the Institut für Experimentalphysik of the University of Hamburg for their support, and especially the design and technical construction team, B. Frensche and J. Pelz, as well as the head of the mechanical workshop, S. Fleig, and his entire team for their competent work.

The authors are grateful to W. Hillert, F. Frommberger and the entire ELSA team for their support during the testbeam period, for realising special beam requests and for many helpful discussions concerning a multitude of different ELSA technicalities. Further thanks go to K. Desch, J. Kaminski, D. Elsner, and many others for help and support with the planning and setup before, during, and after the two weeks in Bonn.

The authors acknowledge the financial support of the Deutsche Forschungsgemeinschaft in the DFG project Li 1560/1-1 as well as the complementary support by the Initative and Networking Fund of the Helmholtz Association, contract HA-101 ("Physics at the Terascale").

References

[1] The ILC Collaboration, *"ILC Reference Design Report, Volumes 1-4"*
"1: Executive Summary," J. Brau, Y. Okada, N. Walker (eds.) [arXiv:0712.1950 physics.acc-ph];
"2: Physics at the ILC," A. Djouadi, J. Lykken, K. Mönig, Y. Okada, M. Oreglia, S. Yamashita (eds.) [arXiv:0709.1893 hep-ph];
"3: Accelerator," N. Phinney, N. Toge, N. Walker (eds.) [arXiv:0712.2361 physics.acc-ph];
"4: Detectors," T. Behnke, C. Damerell, J. Jaros, A. Miyamoto (eds.) [arXiv:0712.2356 physics.ins-det].

[2] G.A. Moortgat-Pick *et al.*, Phys. Rept. **460** (2008) 131, [arXiv:hep-ph/0507011].

[3] The ALEPH, DELPHI, L3, OPAL and SLD Collaborations, the LEP and SLD Electroweak Working Groups and the SLD Heavy Flavour Group, Phys. Rept. **427** (2006) 257; [arXiv:hep-ex/0509008].

[4] S. Boogert *et al.*, JINST **4** (2009) P10015. [arXiv:0904.0122v2 physics.ins-det].

[5] V. Gharibyan, N. Meyners, and K.P. Schüler, TESLA Report 2001-23, Part III, LC-DET-2001-047, DESY, February 2001; DESY 2001-011, March 2001

[6] E. Fokitis *et al.*, Nucl. Phys. Proc. Suppl. **44** (1995) 246,
E. Albrecht *et al.*, *"VUV Absorbing Vapours in n-Perfluorocarbons,"* CERN-EP/2002-099.

[7] A. Bideau-Mehu *et al.*, J. Quant. Spectrosc. Radiat. Transf. **25** (1981), 395.

[8] The GEANT4 Collaboration, Nucl. Instrum. Meth. A **506**, Issue 3 (2003), 250-303;
The GEANT4 Collaboration, IEEE Trans. Nucl. Science 53 No. 1 (2006), 270-278; ISSN: 0018-9499

[9] The GEANT4 Collaboration, *"*GEANT4 *– Physics Reference Manual,"*
`http://geant4.web.cern.ch/geant4/UserDocumentation/UsersGuides/PhysicsReference` ...
`Manual/fo/PhysicsReferenceManual.pdf` (cont'd)

[10] C. Bartels *et al.*, Poster *"Photodetector Studies and Prototype Simulation of a Cherenkov Detector for an ILC Polarimeter,"* IEEE 2008 Nuclear Science Symposium and Medical Imaging Conference, Dresden, Germany, October 2008.

[11] C. Helebrant, Nucl. Instrum. Meth. A **610** (2009) 387.

[12] C. Helebrant, *"In Search of New Physics Using Polarization – HERA and ILC,"* Ph.D. Thesis, University of Hamburg, Hamburg, Germany, 2009.

[13] HAMAMATSU PHOTONICS K.K. (`http://sales.hamamatsu.com/` abbrev. as `~hamamatsu/`)
R7600U-03-M4 (2007): `~hamamatsu/assets/pdf/parts_R/R5900U_R7600U_TPMH1291E03.pdf`
R7600-00-M64 (2006): `~hamamatsu/index.php?id=13195917`
R7400U-06(03) (2004): `~hamamatsu/assets/pdf/parts_R/R7400U_TPMH1204E07.pdf`

[14] PerkinElmer, Lambda 800 Spectrometer
`http://las.perkinelmer.com/Catalog/default.htm?CategoryID=Lambda+800+Spectrometer`

[15] PHOTONIS USA
XP1911/UV (1999): `http://www.photonis.com/upload/industryscience/pdf/pmt/XP1911UV.pdf`

[16] Agilent Technologies, LED of type: HLMP-CB30-NRG00
Datasheet: `http://www.chipcatalog.com/Agilent/HLMP-CB30-NRG00.htm`

[17] W. Hillert, Eur. Phys. J. A **28S1** (2006) 139.

wavelength	R_{diam}	R_{roll}
160 nm	74 %	11 %
180 nm	77 %	18 %
200 nm	81 %	27 %
220 nm	84 %	30 %
240 nm	86 %	37 %
500 nm	85 %	40 %
520 nm	84 %	39 %
650 nm	83 %	40 %
900 nm	82 %	39 %

Table 1: *The reflectivities of diamond-milled quality aluminium R_{diam} and of rolled quality aluminium R_{roll} as determined with the* PerkinElmer *spectrometer and implemented in the* Geant4 *simulation.*

photodetector types	sensitive area in [mm^2]	wavelength range [nm]	typical gain	response time	anode pads
R7600U-03-M4 [(a)]	18.0×18.0	185 - 600	$1.8 \cdot 10^6$	11.0 ns	4
R7600-00-M64 [(a)]	18.1×18.1	300 - 600	$0.3 \cdot 10^6$	13.4 ns	64
R7400U-06(03) [(a)]	$\varnothing = 8$ mm	160(185) - 600	$0.7 \cdot 10^6$	6.5 ns	1
XP1911/UV [(b)]	$\varnothing = 15$ mm	200 - 600	$0.9 \cdot 10^6$	28.0 ns	1

Photodetector from: (a) Hamamatsu, (b) Photonis.

Table 2: *Key characteristics of the four different photomultipliers from* Hamamatsu *and* Photonis *[13, 15]. The two MAPMs (R7600U-03-M4 and R7600-00-M64) have a quadratic cross-section of similar size, but differ in the number of anodes and in their wavelength range. The two SAPMs (R7400U-03 and R7400U-06) differ in the size of their sensitive areas and slightly in wavelength range.*

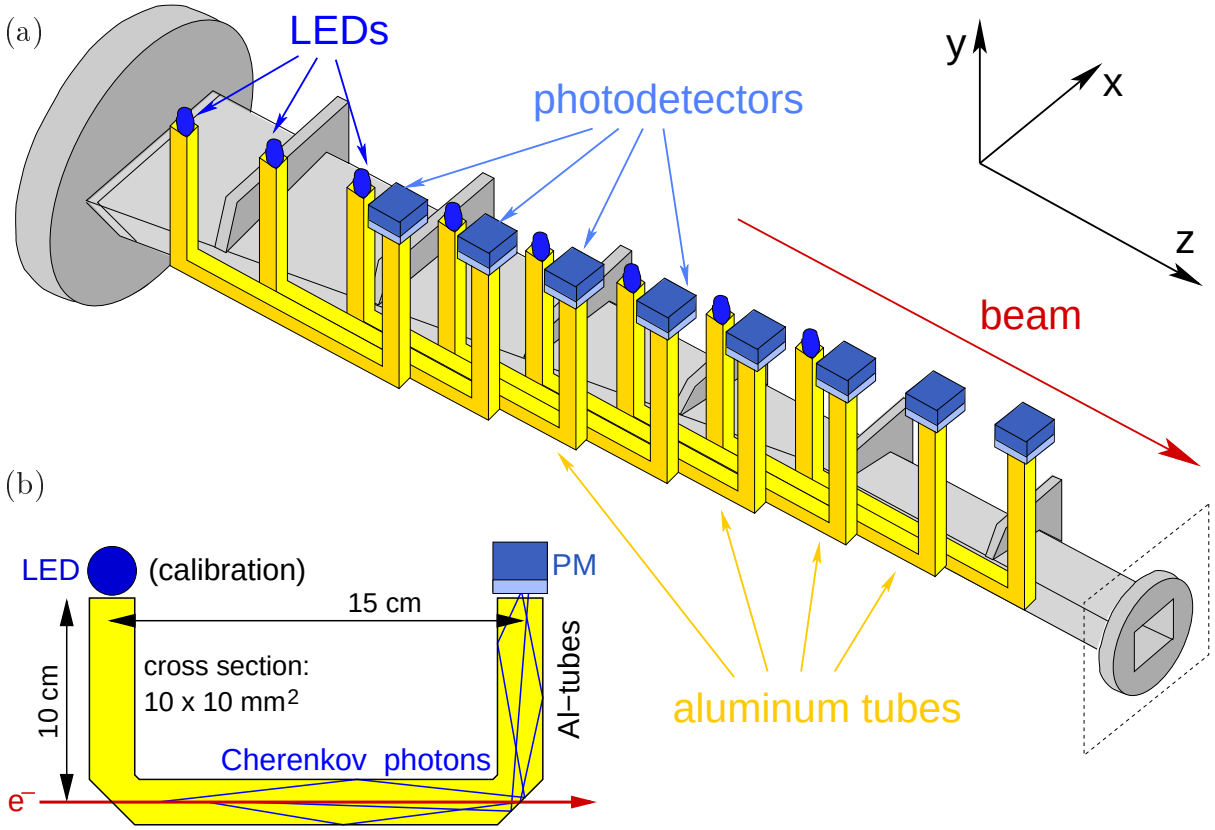

Figure 1: *(a) Illustration of a Cherenkov detector for ILC polarimetry, here for better visibility with eight instead of the actually forseen 20 readout channels; and (b) sketch of one such gas-filled aluminium channel.*

Figure 2: *Event display of the prototype simulation:*
The electron beam (red) passes from left to right through the U-base of the aluminium tubes filled with perfluorobutane, C_4F_{10}, and emits Cherenkov photons (green). These are reflected upwards to a photodetector mounted on the hind U-leg. Both channels are separated by a thin foil (light grey).
Due to a surrounding gas-filled box (not shown), Cherenkov radiation can also be emitted before/after the electron beam enters/exits the aluminium tubes, but it cannot reach the photodetector.

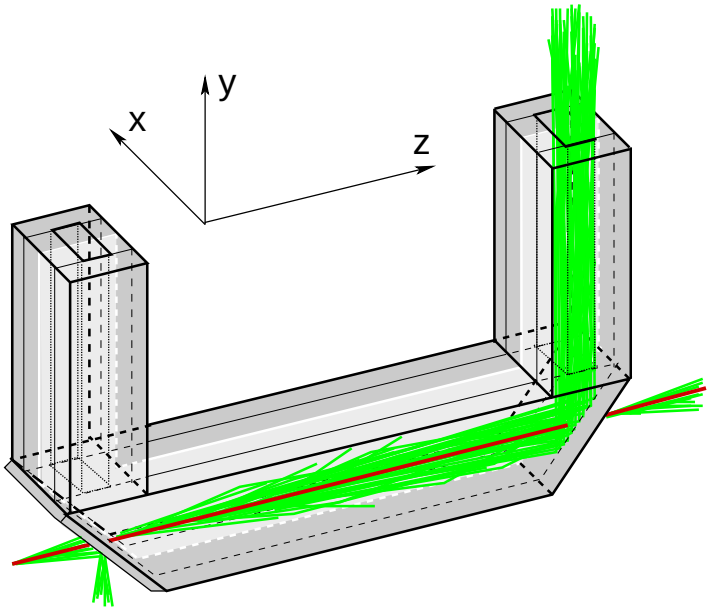

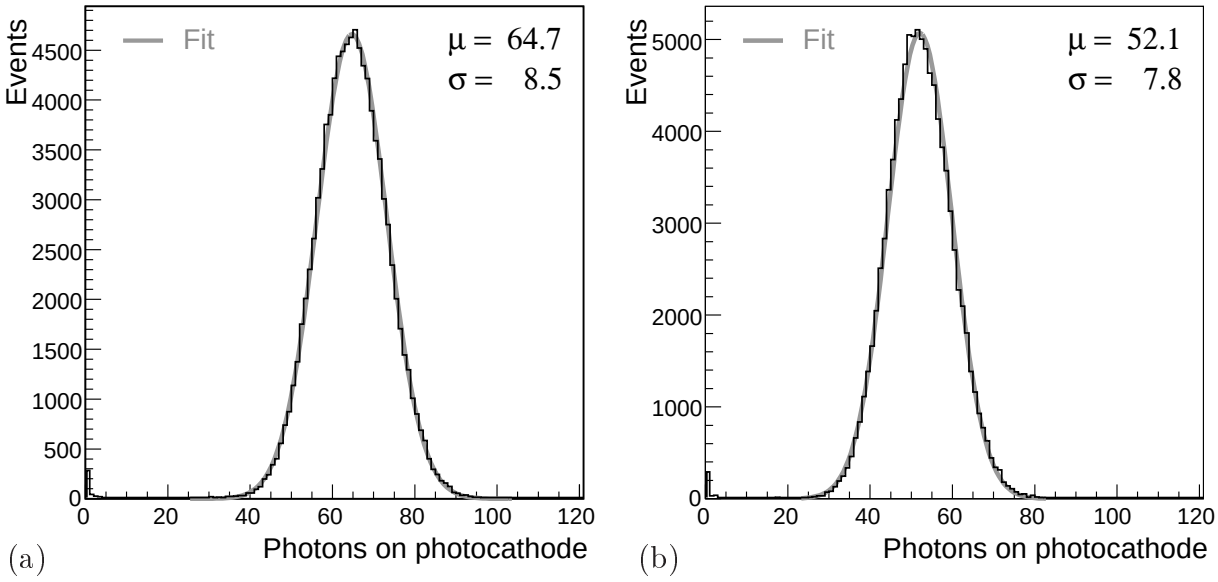

Figure 3: *Average number of photons reaching the photocathode per Compton electron: (a) with equal reflectivities for all channel walls and (b) with a reduced reflectivity of the inter-channel wall.*

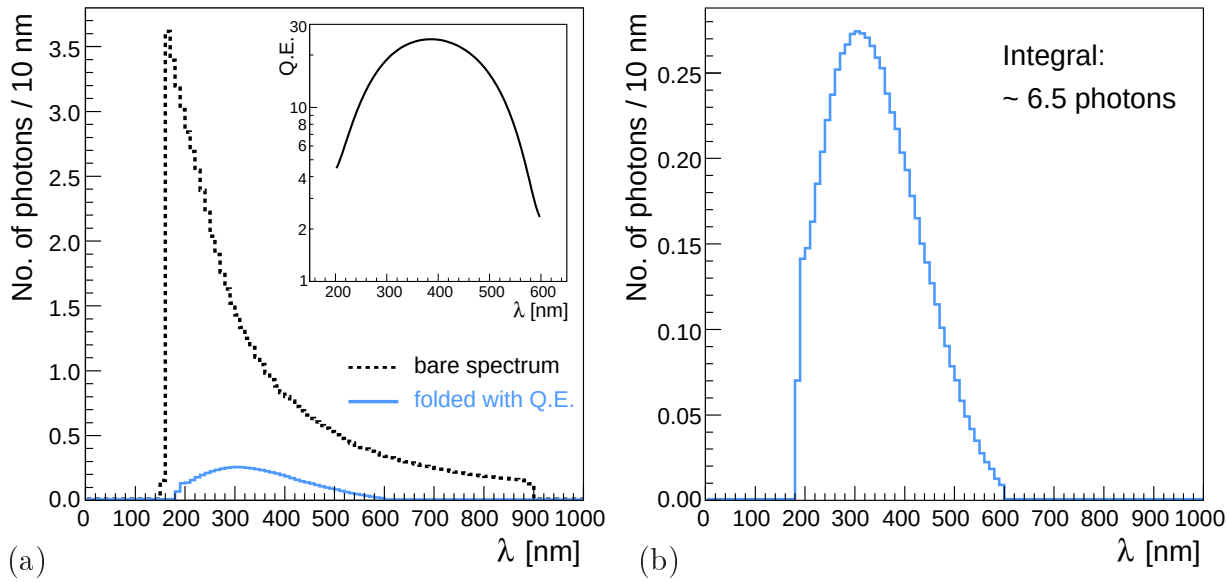

Figure 4: *Cherenkov spectra: (a) at the photocathode (dotted line) and (b) convoluted with the quantum efficiency (Q.E.) of the 2×2 MAPM (R7600U-03-M4), see the insert in (a). The convoluted spectrum is also superimposed in (a) as the solid line.*

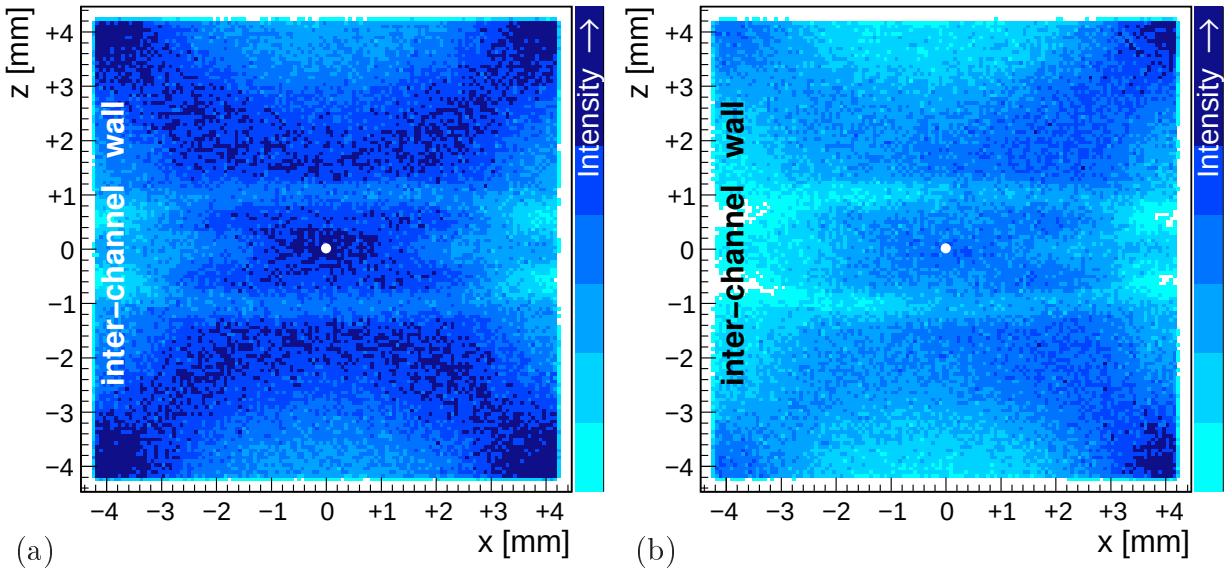

Figure 5: *Light distribution on the photocathode: (a) with equal reflectivities for all channel walls, (b) with a reduced reflectivity for the inter-channel wall at $x = -4.25\,\mathrm{mm}$. The white dot indicates the channel centre; the intensity scale ranges from 40% to 100%.*

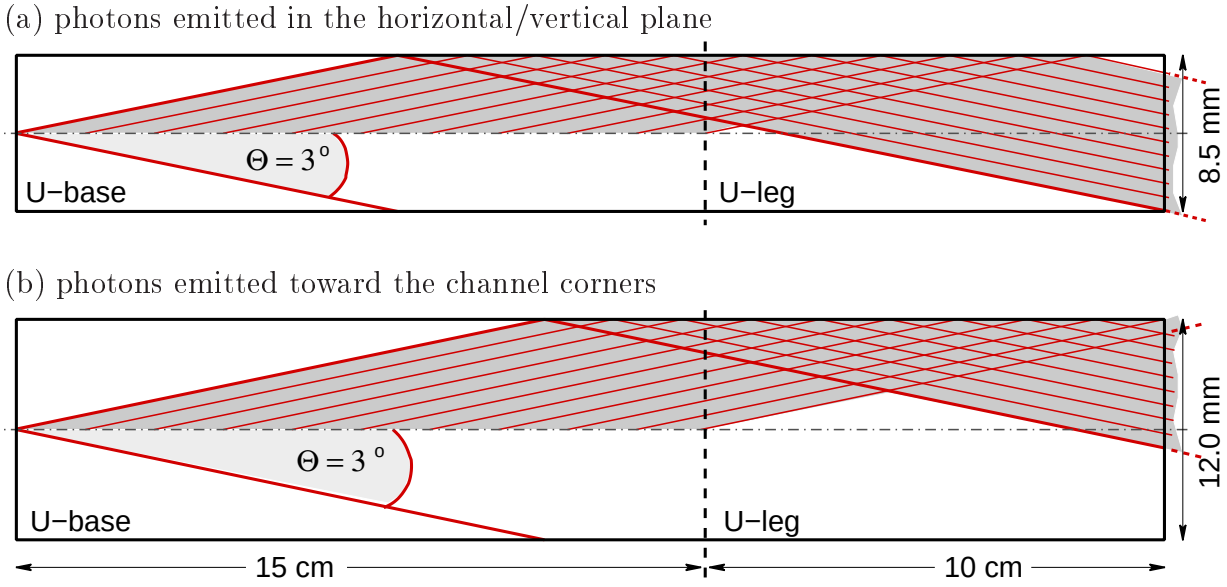

Figure 6: *Sketches of possible light paths for electrons traversing the channel along the central axis and the Cherenkov angle of the chosen gas ($\Theta = 3°$). The channel aspect ratio has been enlarged by a factor of 4 for better visibility.*
(a) Photons emitted in the horizontal/vertical plane illuminate the entire channel width at the photocathode, while (b) photons emitted towards the channel corners only illuminate half the channel width. The 90° reflection at the end of the U-base (indicated by the vertical dashed line) has no influence on the symmetry of the distribution.

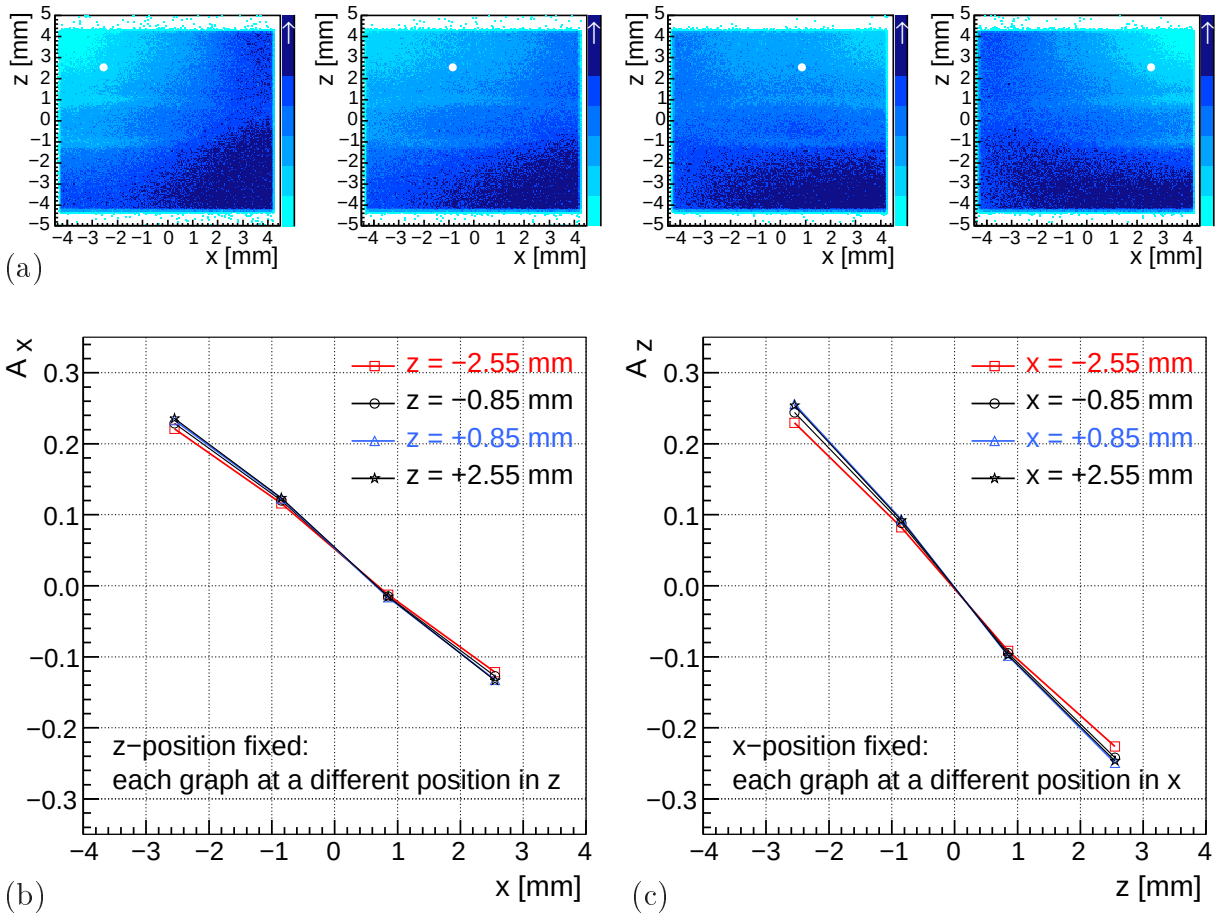

Figure 7: *(a) Simulated light yield at the photocathode for a horizontal beam position scan at* $z = +2.55\text{mm}$. *The* x *and* z *asymmetries have been calculated from horizontal and vertical scans using* 10^4 *electrons for each beam position: (b)* A_x *for different* z*-positions and (c)* A_z *for different* x*-positions.*

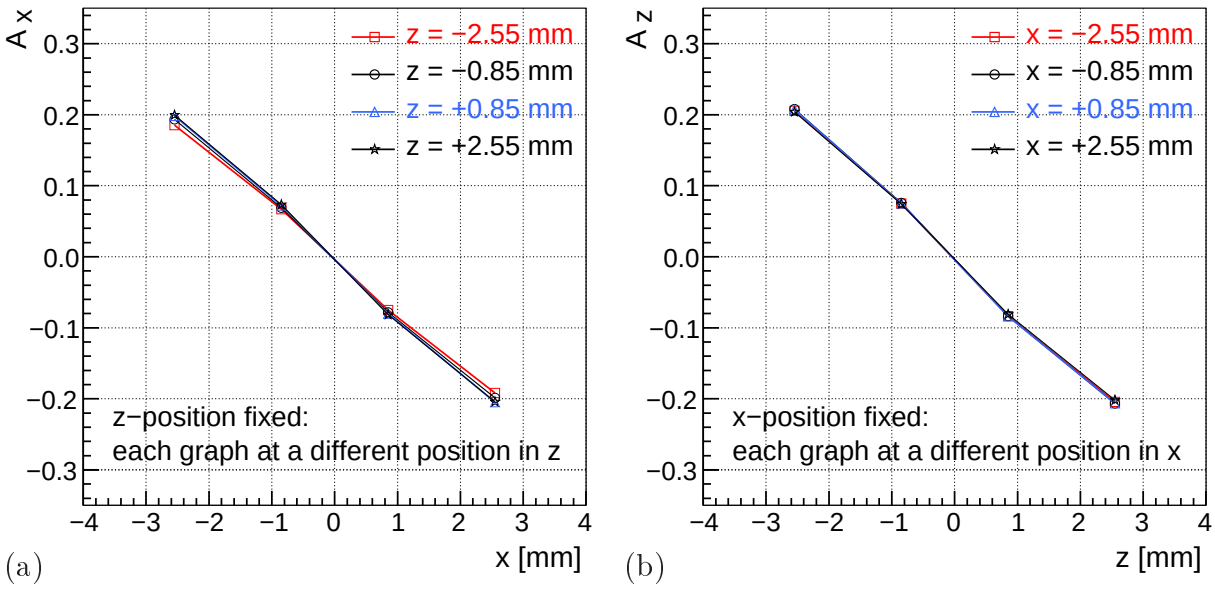

Figure 8: *Asymmetries obtained with equal reflectivities for all inner channel walls: (a) A_x and (b) A_z for different z- and x-positions, respectively. Compare Figure 7 (b, c) with a reduced reflectivity for the inter-channel wall.*

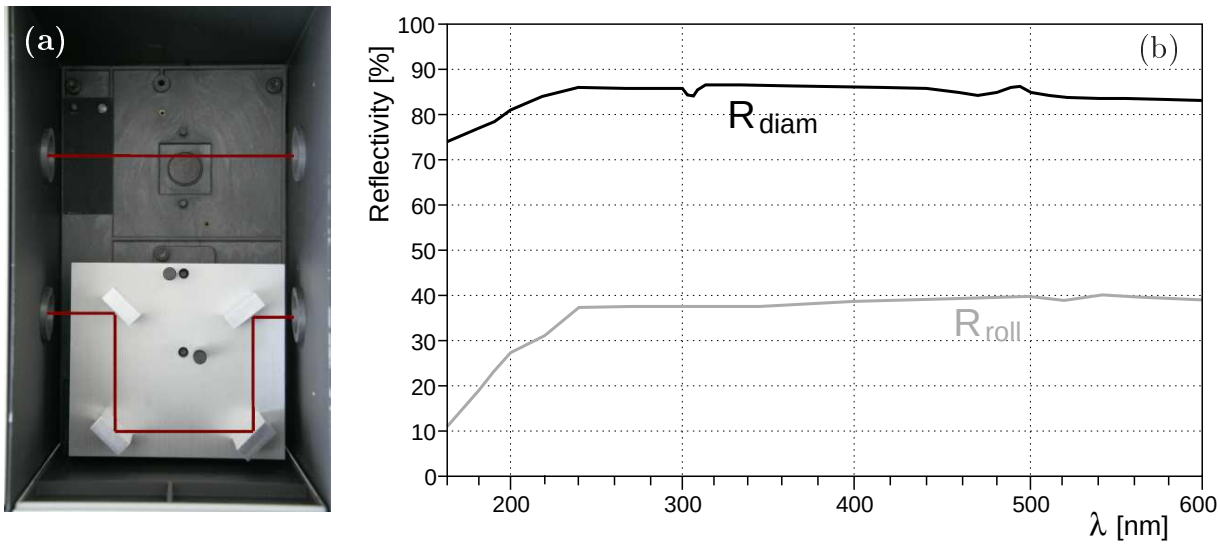

Figure 9: *(a) Photograph of the interior of the modified* PerkinElmer *transmission spectrometer with the indicated paths of the reference beam (top) and the measurement beam (bottom). (b) Measured reflectivities of diamond-milled aluminium (upper line) and of rolled aluminium (lower line).*

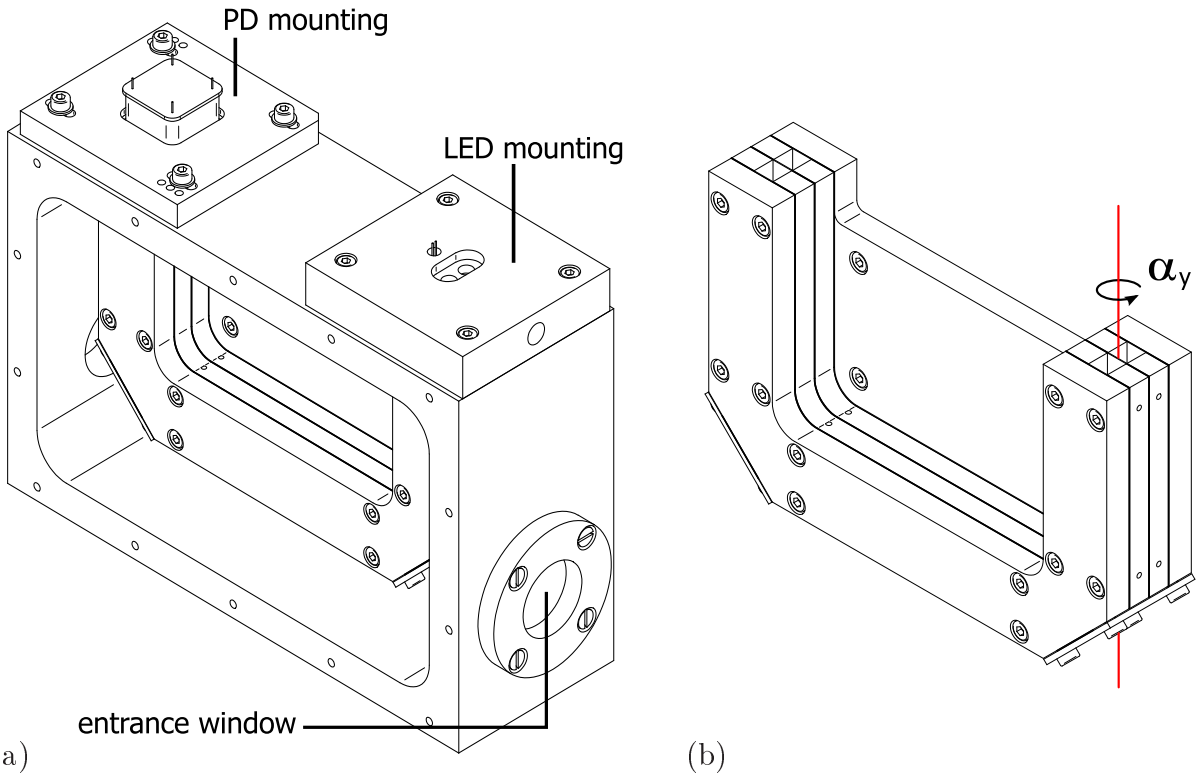

(a) (b)

Figure 10: *Parts of a technical drawing for the assembly of the prototype: (a) the box base body, already including the channel structure (b) of two parallel U-shaped channels.*

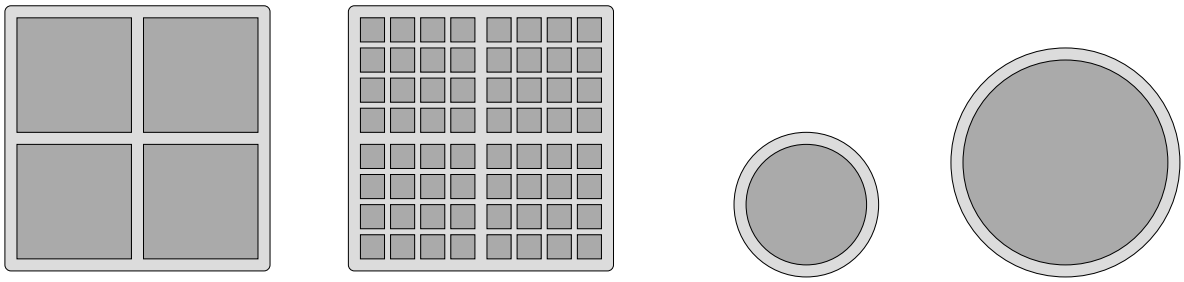

(a) M4: 2×2 MAPM (b) M64: 8×8 MAPM (c) R7400U (d) XP1911/UV

Figure 11: *Anode schemes of the different multi- and single-anode photomultiplier types, in correct relative scaling.*

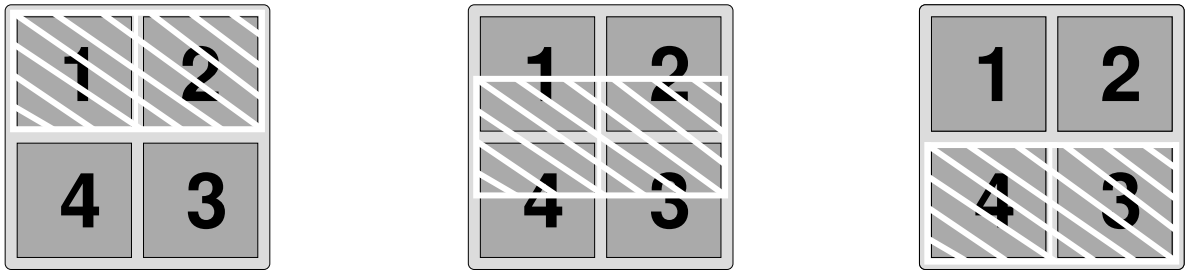

Figure 12: *Different positions of the MAPMs (grey) on the detector channels (hatched).*

Figure 13: *Calibration LEDs covered by POM tubes.*

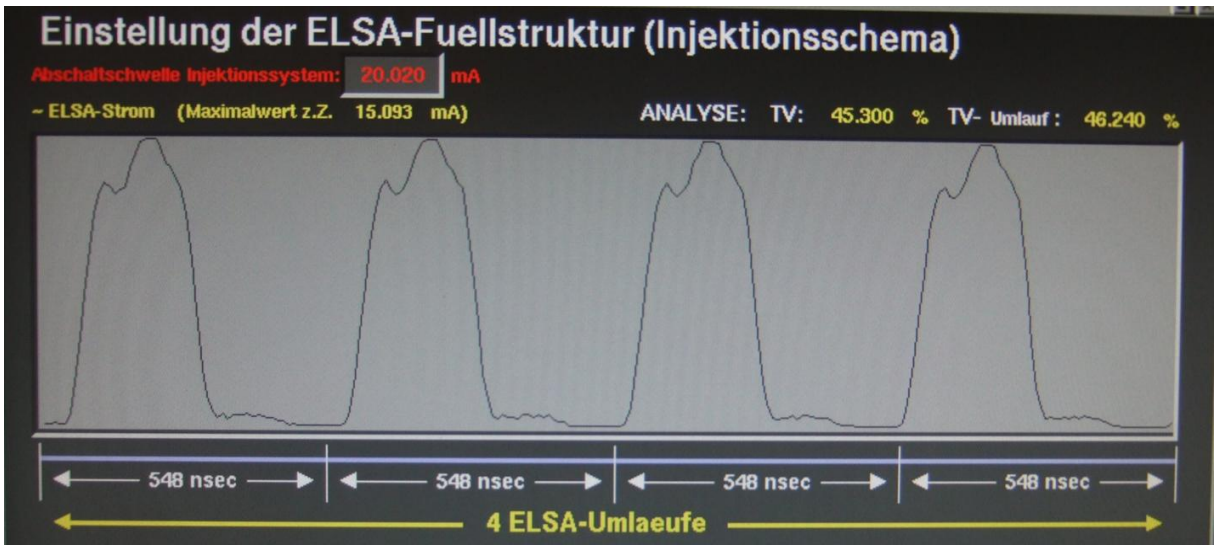

Figure 14: *Example of an ELSA fill structure for four* 548 ns *turns. About half of the available buckets are filled.*

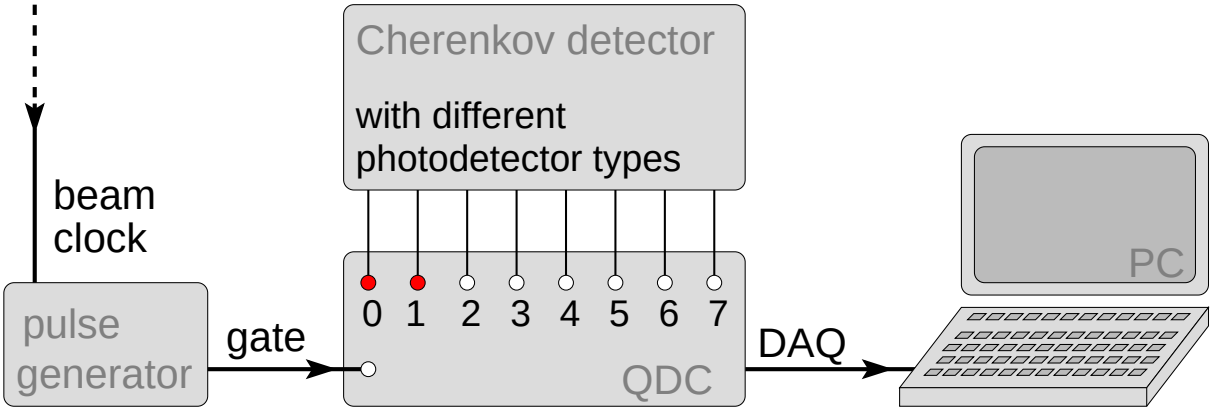

Figure 15: *Block diagram of the readout chain as realised during the testbeam period.*

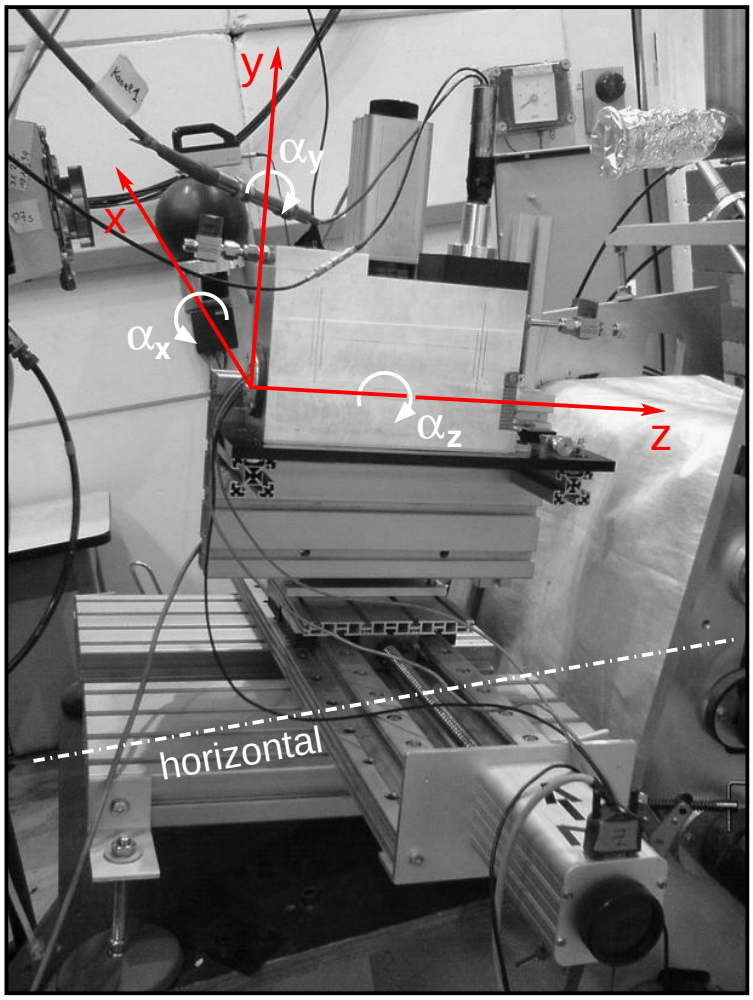

Figure 16: *The prototype Cherenkov detector on its base plate (black, with the rotational mechanism visible on the right) is mounted on a stage moveable along the x- and y-axis.*

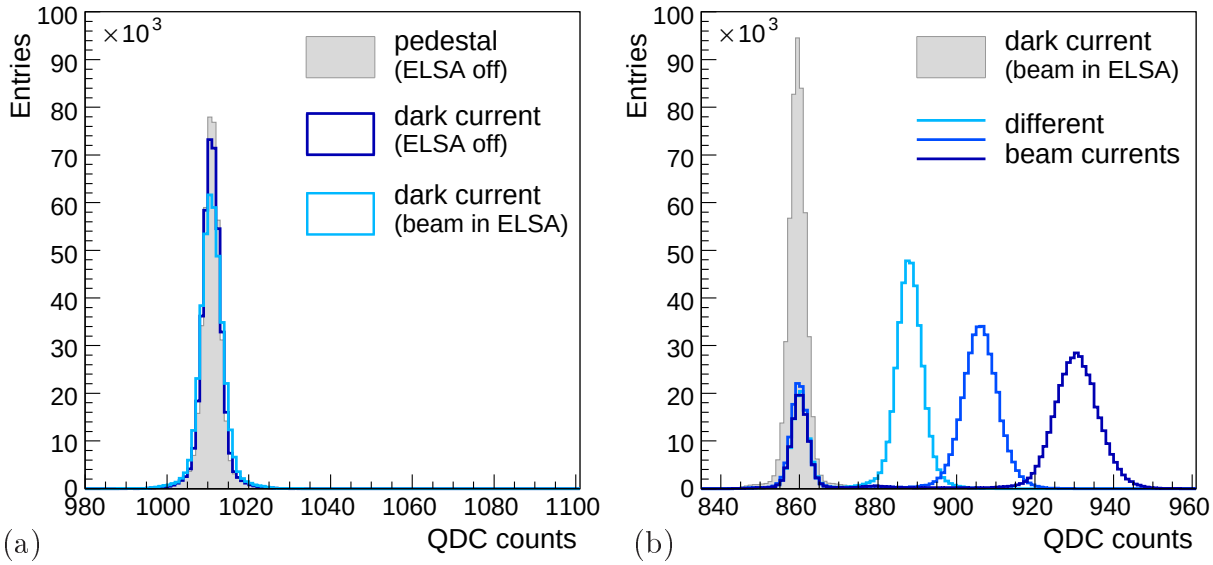

Figure 17: *Data recorded with the 2×2 MAPM (R7600U-03-M4):*
(a) QDC response without bias voltage applied to the photodetector (pedestal) and with 400 V *applied (dark current), both without and with beam circulating in ELSA.*
(b) Cherenkov signals increase with increasing electron beam current, while the pedestal position remains stable. The 4:1 *area ratio between the beam signal peak and the pedestal of each open histogram corresponds to the beam extraction cycle of* 4s:1s.

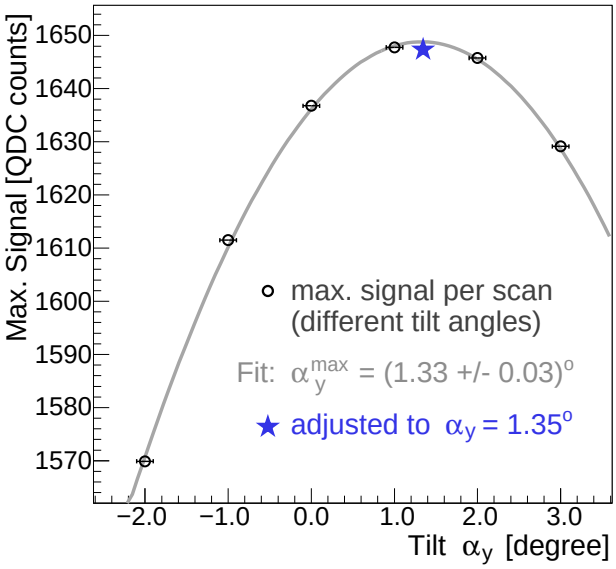

Figure 18: *Detector alignment with the 2×2 MAPM (bias voltage* 860 V*): The tilt in the (x, z)-plane is determined from x-scans for six different tilt angles. An additional measurement for the adjusted tilt of $\alpha_y = 1.35°$ is also displayed.*

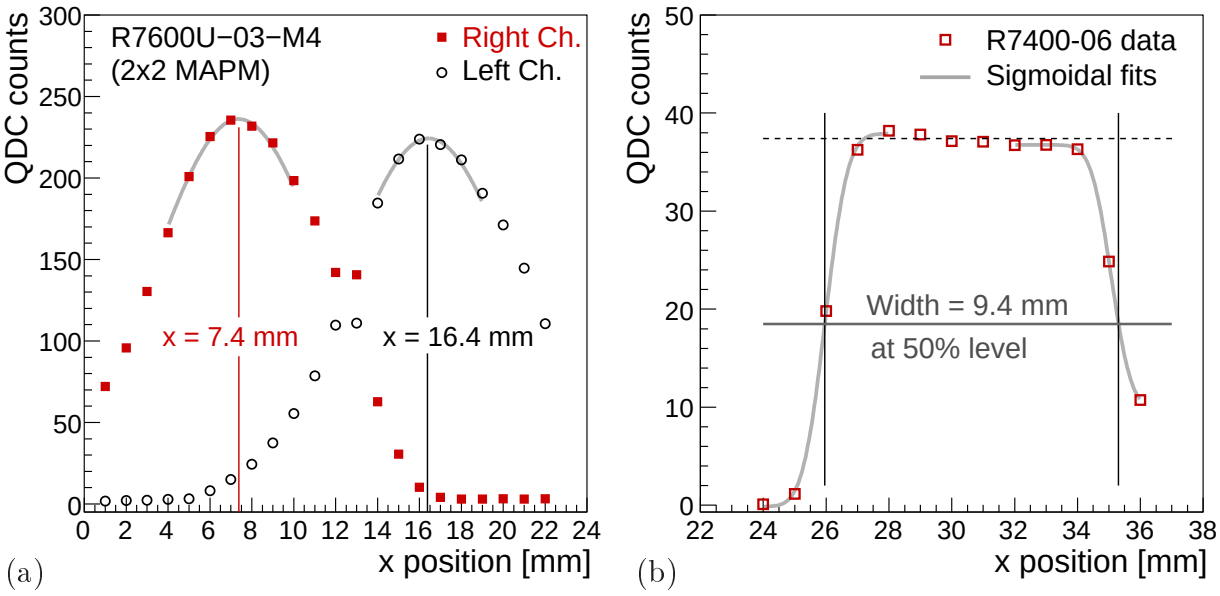

Figure 19: *Results from x-scans for two different types of photomultipliers: (a) the 2×2 MAPM (R7600U-03-M4, bias voltage* 860 V*), (b) the SAPM (R7400U-06, bias voltage* 300 V*). The absolute x-values correspond to different stage zero-positions; only the relative values are relevant.*

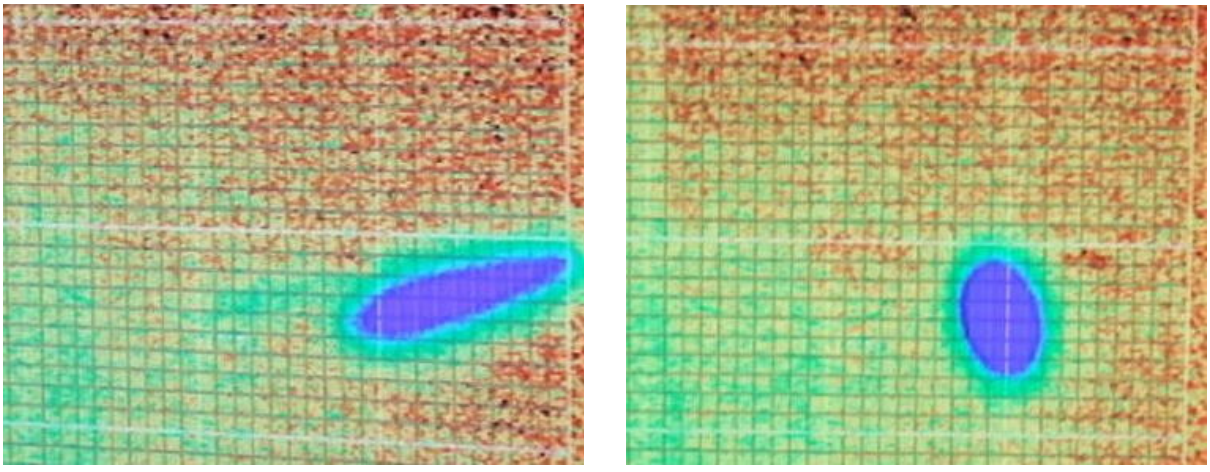

(a) larger, elongated beam spot (b) smaller, nearly round beam spot

Figure 20: *Two beam spot shapes observed at ELSA when (a) the data in Fig. 19(a) and (b) the data in Fig. 19(b) were recorded.*

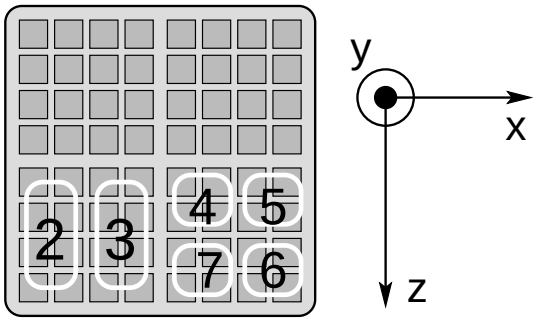

Figure 21: *Readout configuration for the 8×8 MAPM: The anode pads are depicted as grey squares; the readout channels as numbered white rectangles.*

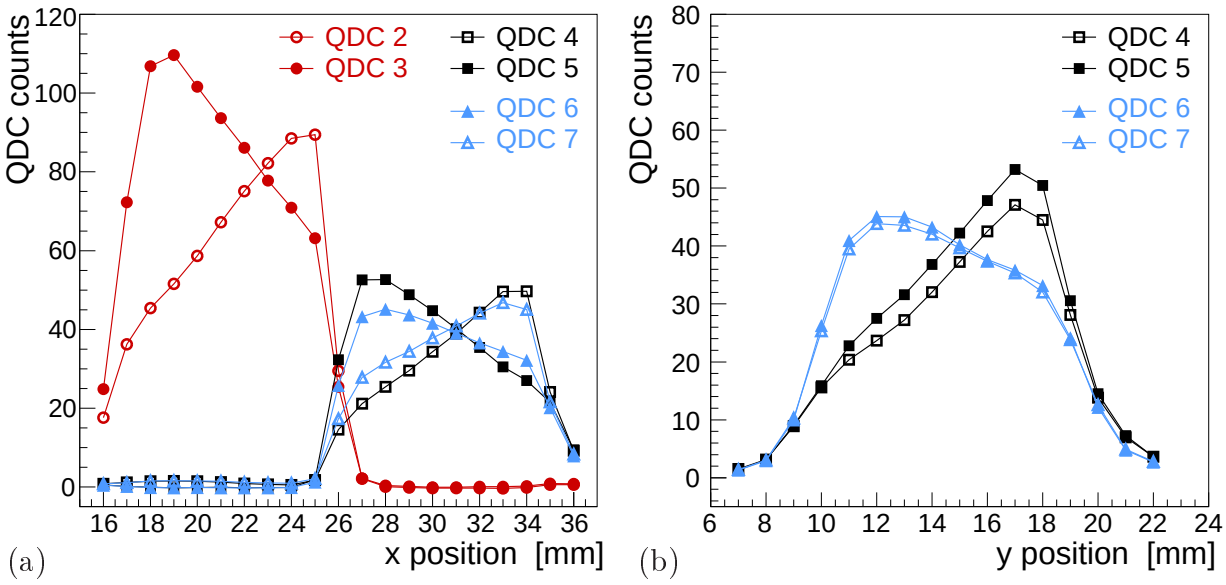

Figure 22: *Beam postion scan data recorded with the 8×8 MAPM (bias voltage 500 V): (a) x-scan across both channels and (b) y-scan on the left channel.*

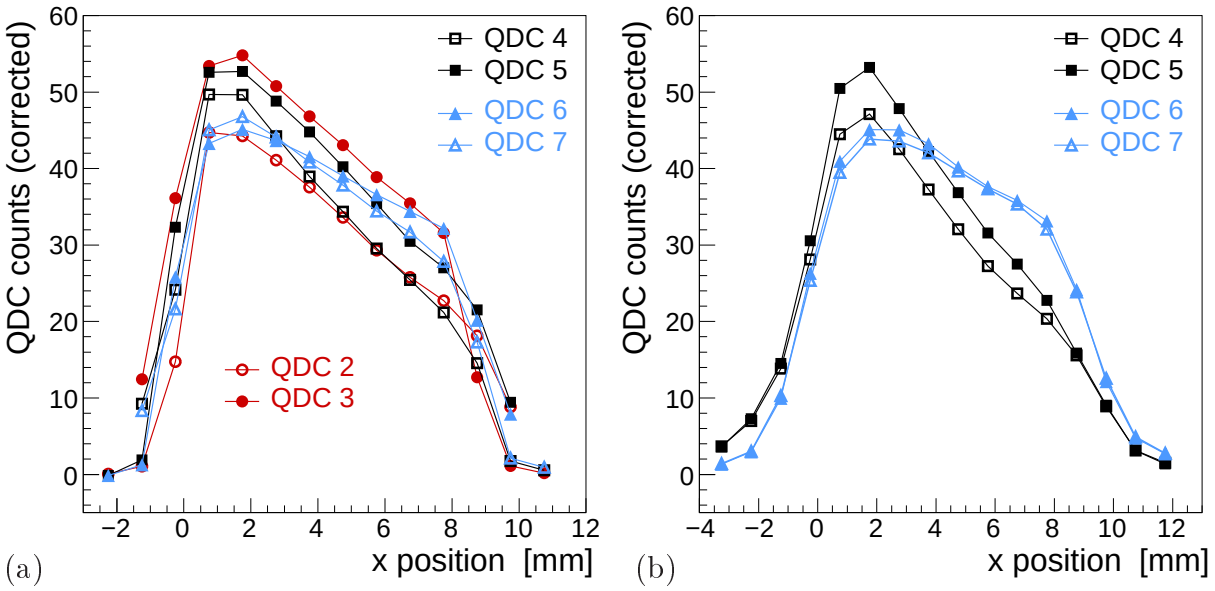

Figure 23: *Different visualisation of the position scan data presented in Figure 22 with the emphasis on shape and amplitude differences: (a) x-scan data and (b) y-scan data.*

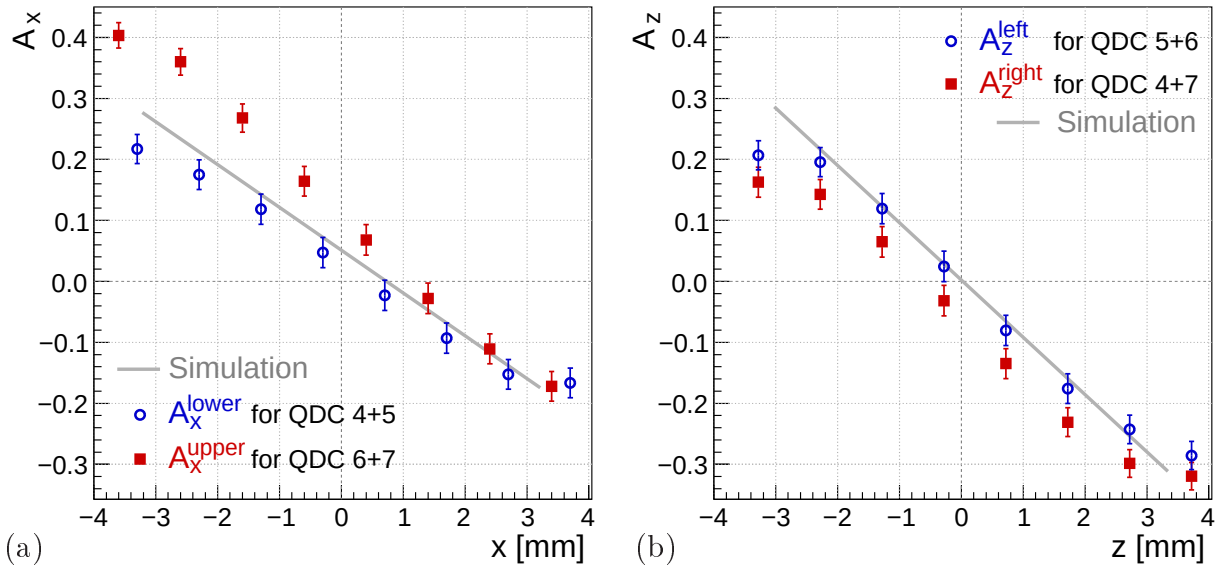

Figure 24: *Asymmetries calculated from the position scan data sets recorded with the 8×8 MAPM: (a) A_x for QDC-pairings 4+5 and 6+7 and (b) A_z for QDC-pairings 4+7 and 5+6. The error bars correspond to 10% relative gain variations between the anode pads.*